



Evaluation of Applicability of a Flare Trigger Model Based on a Comparison of Geometric Structures

Yumi Bamba¹ and Kanya Kusano² 

¹ Institute of Space and Astronautical Science (ISAS)/Japan Aerospace Exploration Agency (JAXA) 3-1-1 Yoshinodai, Chuo-ku, Sagami-hara, Kanagawa 252-5210, Japan; y-bamba@nagoya-u.jp

² Institute for Space-Earth Environmental Research (ISEE)/Nagoya University Furo-cho, Chikusa-ku, Nagoya, Aichi 464-8601, Japan
Received 2017 August 8; revised 2018 January 30; accepted 2018 January 31; published 2018 March 22

Abstract

The triggering mechanism(s) and critical condition(s) of solar flares are still not completely clarified, although various studies have attempted to elucidate them. We have also proposed a theoretical flare-trigger model based on MHD simulations in which two types of small-scale bipole fields, the so-called opposite polarity (OP) and reversed shear (RS), can trigger flares. In this study, we evaluated the applicability of our flare-trigger model to the observation of 32 flares that were observed by the *Solar Dynamics Observatory*, by focusing on geometrical structures. We classified the events into six types, including the OP and RS types, based on photospheric magnetic field configuration, presence of precursor brightenings, and shape of the initial flare ribbons. As a result, we found that approximately 30% of the flares were consistent with our flare-trigger model, and the number of RS-type triggered flares is larger than that of the OP type. We found that none of the sampled events contradict our flare model; though, we cannot clearly determine the trigger mechanism of 70% of the flares in this study. We carefully investigated the applicability of our flare-trigger model and the possibility that other models can explain the other 70% of the events. Consequently, we concluded that our flare-trigger model has certainly proposed important conditions for flare-triggering.

Key words: Sun: flares – Sun: magnetic fields – sunspots

Supporting material: tar.gz file

1. Introduction

A solar flare is a sudden release of magnetic energy in the solar corona, and it is widely accepted that flare occurrence is related to topological changes of the magnetic field, such as that caused by magnetic reconnection (see CSHKP model, Carmichael 1964; Sturrock 1966; Hirayama 1974; Kopp & Pneuman 1976). Two major physical models of solar eruptions, including flares and coronal mass ejections (CMEs), have been proposed so far: “ideal magnetohydrodynamics (MHD) models” and “magnetic reconnection models.” They emphasize different aspects of the mechanism of solar eruptions. The ideal MHD models point out that some ideal MHD instabilities cause the onset of solar eruptions. For instance, the torus instability (e.g., Bateman 1978; Kliem & Török 2006; Démoulin & Aulanier 2010; Kliem et al. 2014), or helical kink instability (e.g., Gerrard et al. 2001; Fan & Gibson 2003; Török et al. 2004; Török & Kliem 2005), has been proposed as the mechanism of solar eruptions. The torus instability is determined by the decay rate of the external poloidal field B_{ex} , and the critical condition is defined by the decay index $n = -d(\ln B_{\text{ex}})/d(\ln R)$. Recently, the critical range for the onset of the torus instability is proposed as $n \sim 1.3\text{--}1.5$ (Zuccarello et al. 2015). Some observational and computational studies using nonlinear force-free field (NLFFF; e.g., Cheng et al. 2011; Kliem et al. 2013; Savcheva et al. 2015) modeling support the torus instability; though, the torus instability required an external agent that lifts the flux rope to an unstable height range. The helical kink instability model proposes that solar eruptions are caused by growth of the helical kink instability. The helical kink instability can grow when magnetic twist becomes strong enough, and it can grow even if a twisted flux rope does not reach the critical height of the torus

instability. Hassanin & Kliem (2016) showed a nice comparison between observations and an MHD simulation for a confined M-class flare. Liu et al. (2016) also showed that there is consistency between the helical kink instability mechanisms and sequential confined flares from a combination of observations and NLFFF modeling. However, the helical kink instability requires higher twist in a flux rope and observations do not always show such a high twist.

The ideal MHD models postulate that a flux rope exists prior to eruption, as is mentioned above. On the other hand, magnetic reconnection models note that some kind of magnetic reconnection causes the onset of a solar eruption. Two kinds of reconnection models have been proposed so far. One is the “magnetic breakout model” (Antiochos et al. 1999; Karpen et al. 2012) and the other is the “tether-cutting model” (Moore et al. 2001; Moore & Sterling 2006). The magnetic breakout model considers a multi-flux topology that consists of multiple flux systems with a coronal null point (e.g., Priest & Titov 1996; Sun et al. 2012). Sheared magnetic arcades can be created through many means such as slow photospheric shear. This leads to the storage of free energy. Breakout reconnection can then remove the overlying magnetic field, and the core magnetic flux is free to erupt. Reva et al. (2016) showed breakout reconnection associated with a CME using observations from the TESIS EUV telescope. The tether-cutting model proposes that magnetic reconnection in the core of a sheared magnetic arcade creates a flux rope and causes the eruption. Liu et al. (2013) showed evidence of tether-cutting reconnection using a NLFFF model using solar observational data of a flare productive AR. The breakout and tether-cutting models are clearly reviewed from an observational perspective in Schmieder et al. (2015).

There are various studies trying to find out what observable parameter(s) determine flare and solar eruption onset condition (s), while various models are proposed from computational studies and have been validated by observations, as mentioned above. One such model is flux cancellation (van Ballegoijen & Martens 1989; Aulanier et al. 2010), whose basic concept is that tether-cutting reconnection forms a flux rope and it partially cancels magnetic flux in the core of a sheared arcade causing the MHD instability to be triggered. Green et al. (2011) clearly showed flux cancellation and associated flux rope formation in the photosphere prior to an eruption. Another model is the emerging flux model proposed by Chen & Shibata (2000). They considered two cases based on the positional relationship between emerging flux and a flux rope. If emerging flux appears below a flux rope (i.e., on the polarity inversion line: PIL) and partial magnetic cancellation occurs, local magnetic pressure is decreased and the pressure gradient causes upflow that pushes the flux rope upward to erupt. On the other hand, if a flux rope appears beside the overlying field (i.e., away from the PIL), the overlying field that prohibits the flux rope from eruption is weakened by magnetic reconnection with the emerging flux, and the flux rope may erupt. Many other studies proposed various magnetic properties that seem to relate to the onset of solar eruptions, such as the length of highly sheared PILs (Hagyard et al. 1984b), magnetic flux close to high gradient PILs (Schrijver 2007), free magnetic energy based on the presence of strong gradient PILs (Falconer et al. 2008), area and total magnetic flux in an active region (AR; Higgins et al. 2011), and total unsigned current helicity over an AR (Bobra & Couvidat 2015), etc. However, it is still unclear what triggers the MHD instability or magnetic reconnection that leads to an eruption.

Although each model proposed a solar eruption scenario, it is likely that the eruption onset results from the feedback and interaction of different processes. For instance, Hagyard et al. (1984a) suggested that an overall instability driving energy release results from the positive feedback between reconnection and eruption of the sheared field. Kusano et al. (2012; henceforth “K12”) numerically demonstrated the feedback model in which positive feedback between an ideal MHD instability and magnetic reconnection causes explosive growth of solar eruptions. Their basic idea is that “internal magnetic reconnection” between different spatial-scale magnetic fields (between a large-scale sheared field and a small-scale bipole field) forms a double-arc twisted loop and triggers reconnection among the large-scale sheared fields by destabilizing the double-arc twisted loop. In fact, Ishiguro & Kusano (2017) recently showed that the double-arc twisted loop becomes unstable if the parameter κ , given by the product of magnetic twist and the fraction of reconnected flux, exceeds a threshold. Their model is consistent with the tether-cutting reconnection scenario and explains the physical process from the theoretical point of view. K12 proposed that the feedback interaction can be triggered by reconnection between magnetic fields of different spatial-scales if two geometrical parameters—the sheared angle θ_0 of a large-scale field and the azimuth φ_e of a small-scale bipole field—satisfy some condition. We briefly review the K12 model later in Section 2.1 and Figure 1. They surveyed combinations of θ_0 and φ_e and found that there are two specific cases; the opposite polarity (OP) and reversed shear (RS) fields, which can trigger a flare. The essence of the K12 model is that a positive feedback interaction of an ideal

MHD instability and flare reconnection can be triggered by the two types of small-scale “trigger fields.” Bamba et al. (2013) developed a way to measure the angles θ_0 and φ_e using the photospheric magnetic field and chromospheric brightenings observed by the *Hinode* satellite (Kosugi et al. 2007). They found that either the OP- or RS-type magnetic field condition was satisfied prior to several major flares.

In this study, we aim to evaluate the consistency between the flare-trigger condition of K12 and observations, focusing on geometrical structures. For that purpose, we investigate more flares than Bamba et al. (2013) since only a small number of flares were studied in their papers. Specifically, we determine what fraction of the flares are consistent with the OP or RS types and whether a flare occurred with some condition other than OP or RS fields. We increased the number of events analyzed to 32. This was possible due to the large field of view (FOV) of the *Solar Dynamics Observatory* (SDO; Pesnell et al. 2012).

The paper is organized in the following manner. We first review the theoretical model of K12, which we focused on in this study, and describe the data analysis methods and event selection criteria in Section 2. Then we classified the events into six different types, including the OP and RS types, based on the analysis, and describe distinctive features for each type in Section 3. In Section 4, we discuss other possibilities than K12’s model for triggering some specific types of events, which we classified in this study, and discuss caveats to the analysis identifying the flare-triggering site. We finally summarize the conclusions of the present study in Section 5.

2. Data Analysis and Event Classification

2.1. Synopsis of the Theoretical Model

We briefly review the theoretical model proposed by K12. The model simplifies the magnetic field structure of an AR and quantitatively surveyed magnetic configurations that can produce solar eruptions (flares). Figure 1(a) shows their simulation setup. They imposed a small bipole field onto the PIL of the large-scale bipole field representing an AR. The internal magnetic reconnection can occur between the sheared field (red arcade) and the small-bipole field (blue arcade), and it precedes flare reconnection among the large-scale sheared fields (red arcades) distributed along the PIL if some condition is satisfied. The surveyed parameters, which describe whether flares occur or not, are θ_0 and φ_e —defined as illustrated in both panels (a) and (b). θ_0 is the angle of the magnetic field relative to the potential field and it increases counter-clockwise in the range of 0° – 90° . φ_e is the counter-clockwise rotation angle of the small-scale bipole field relative to the large-scale potential field in the range of 0° – 360° . The parameters θ_0 and φ_e correspond to the magnetic twist and complexity of the magnetic field, respectively. The combination of (θ_0, φ_e) characterizes the flare-trigger conditions, and either the OP- or RS-type bipole field can trigger the positive feedback process of an MHD instability and magnetic reconnection, leading to flares (and sometimes CMEs). The pre-existing sheared fields connect via the OP-type field and form a double-arc twisted flux rope, then an eruptive MHD instability is triggered and the instability causes flare reconnection, i.e., “eruption-induced reconnection” starts. If the RS type of field exists, a part of the pre-existing sheared field is cancelled by reconnection with the RS field in the core region, and the sheared field collapses

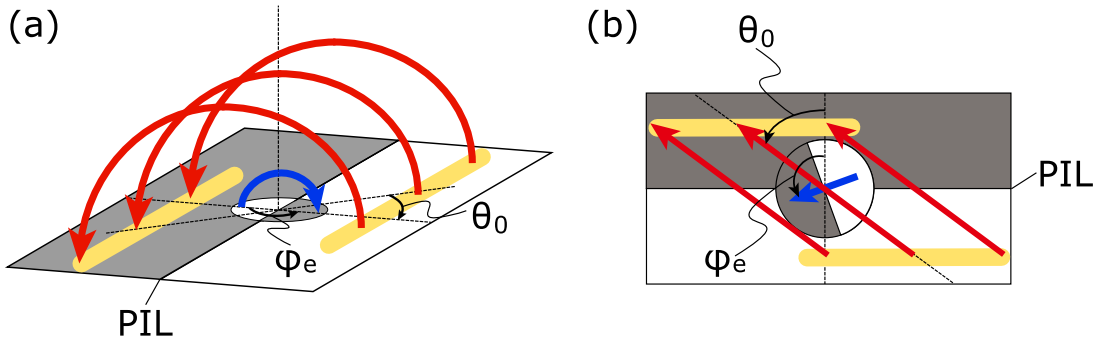


Figure 1. Schematic of the simulation setup in K12 and definition of the angles θ_0 and φ_e . White/black parts represent the positive/negative polarity sunspot of an AR. Red and blue arrows indicate the large-scale sheared field and small-scale bipole field that can be the trigger of a flare, respectively. The thick yellow line illustrates two sheared flare ribbons. (a) Bird's-eye view. (b) Top view.

inward because magnetic pressure is decreased. Then flare reconnection is triggered and the twisted flux rope erupts. It can be described as a “reconnection-induced eruption” process since the erupting flux rope is formed after the flare reconnection.

Several observables that are relevant to the flare-trigger condition have been derived from the simulations and are summarized below.

- I. The magnetic shear angle θ_0 and the angle structure of the PIL disturbance at small scales φ_e is observed to be consist with the conditions of either the OP or RS type.
- II. Precursor brightenings should be seen near the PIL, where the OP or RS configuration is satisfied. This represents the internal reconnection in the lower atmosphere. Hence it is inferred that precursor brightenings can be observed in any emission line that is formed in the lower atmosphere, for example, the chromosphere.
- III. The flare ribbons, which appear in the initial flare phase, should have a clearly sheared configuration, as illustrated by the thick yellow lines in Figure 1. It results from a theoretical prediction that the flare reconnection can be reinforced by an instability that is driven by large-scale (nonpotential) fields (such as the red arcades in Figure 1).

A sheared two-ribbon structure and precursor brightening on a highly sheared PIL is common in many other models such as flux cancellation, flux emergence, any tether-cutting reconnection, and also magnetic breakout models. The key feature of the K12 model is that the precursor brightening should appear near the local PIL, where the OP or RS conditions are satisfied. It is due to the fact that precursor brightenings may represent local heating caused by the internal reconnection between the pre-existing sheared field and trigger field. Moreover, Bamba et al. (2013, 2014) reported that precursor brightenings were observed in the lower atmosphere from the upper photosphere to the transition region, rather than in the corona. This is consistent with the K12 simulation in which the OP or RS flux is injected from the bottom boundary into the corona. Therefore, in this study, we use the above three features (the geometrical structure of the magnetic field; the precursor brightening in the chromosphere; and initial flare ribbons) to test the K12 model.

2.2. Data Description

We used data obtained by the Helioseismic and Magnetic Imager (HMI; Schou et al. 2012) and the Atmospheric Imaging Assembly (AIA; Lemen et al. 2012), both are on board the

SDO satellite. These instruments observe the full disk of the Sun with a large FOV of $2000'' \times 2000''$. HMI observes the polarization states, Stokes- I , Q , U , and V , in the photospheric Fe I line (6173 \AA) with a spatial resolution of $1''$. In this study, we used the HMI level 1.5 line-of-sight (LOS) magnetograms (`hmi.M_45 s` series) and the Spaceweather HMI Active Region Patch (SHARP, `hmi.sharp_cea_720 s`, Bobra et al. 2014) series, which contains vertical and horizontal components of the photospheric magnetic field. The 180° ambiguity is resolved and magnetic field vectors are remapped to the Lambert Cylindrical Equal-area (CEA) projection for SHARP data. Data cadences are 45 s for the LOS magnetograms and 720 s for SHARP data, respectively. AIA observes the solar atmosphere in 10 EUV and UV channels, but, in this study, we only used the AIA 1600 \AA (continuum and C IV line) images that are sensitive to emission from the upper photosphere and transition region ($\log T \sim 5.0$). The spatial resolution is $1''.5$ and the cadence is 24 s for the 1600 \AA data.

2.3. Analysis Procedure

We followed the analysis method developed in Bamba et al. (2013). The analysis method was developed for *Hinode* data, and Bamba et al. (2014) examined the applicability of the techniques to *SDO* data. Here we summarize the essence of the procedure (see details in Bamba et al. 2013, 2014).

1. We calibrated the HMI level 1.5 LOS magnetograms and AIA level 1.0 images to remove spatial fluctuations (spacecraft jitter) and to resample the HMI and AIA images to the same size.
2. We superimposed the PILs and strong brightening contours seen in AIA images onto the HMI LOS magnetograms. We define the flare-triggering site as a region located where the center of the initially sheared flare ribbons and precursor brightening were seen. In other words, if there is no precursor brightening between the initially sheared flare ribbons, we are not able to define the flare-triggering site for the event.
3. We measured the magnetic shear angle θ_0 along the flaring PIL and azimuth φ_e at the flare-triggering site. θ_0 was measured as the angle of the initially sheared flare ribbons relative to direction N , perpendicular to the averaged PIL and representing the direction of the potential field. The averaged PIL used to determine N was derived from a low-pass filtering of the LOS magnetic field through a Fourier transformation. The

Table 1
Event List

No.	Date	Onset Time (UT)	GOES X-ray Class	AR (NOAA)	Type	Angle(s)
1	2011 Feb 13	17:28	M6.6	11158	Reversed Shear	$\theta_0 \sim 88^\circ, \varphi_e \sim 344^\circ$
2	2011 Feb 15	01:44	X2.2	11158	Reversed Shear	$\theta_0 \sim 86^\circ, \varphi_e \sim 331^\circ$
3	2011 Mar 09	23:13	X1.5	11166	Complicated Ribbon	...
4	2011 Aug 03	13:17	M6.0	11261	Multiple Trigger Candidates	$\theta_0 \sim 51^\circ$
5	2011 Aug 04	03:41	M9.3	11261	Complicated Ribbon	...
6	2011 Sep 06	01:35	M5.3	11283	No-precursor Brightening	$\theta_0 \sim 80^\circ$
7	2011 Sep 06	22:12	X2.1	11283	No-precursor Brightening	$\theta_0 \sim 79^\circ$
8	2011 Sep 07	22:32	X1.8	11283	Complicated Ribbon	...
9	2011 Sep 08	15:32	M6.7	11283	Complicated Ribbon	...
10	2012 Jan 23	03:38	M8.7	11402	Multiple Trigger Candidates	$\theta_0 \sim 20^\circ$
11	2012 Mar 05	02:30	X1.1	11429	No-precursor Brightening	$\theta_0 \sim 60^\circ$
12	2012 Mar 07	00:02	X5.4	11429	Reversed Shear	$\theta_0 \sim 108^\circ, \varphi_e \sim 313^\circ$
13	2012 Mar 07	01:05	X1.3	11429	Reversed Shear	$\theta_0 \sim 68^\circ, \varphi_e \sim 295^\circ$
14	2012 Mar 09	03:22	M6.3	11429	Reversed Shear	$\theta_0 \sim 74^\circ, \varphi_e \sim 333^\circ$
15	2012 Mar 10	17:15	M8.4	11429	Reversed Shear	$\theta_0 \sim 98^\circ, \varphi_e \sim 312^\circ$
16	2012 May 10	04:11	M5.7	11476	Complicated Ribbon	...
17	2012 Jul 02	10:43	M5.6	11515	Complicated Ribbon	...
18	2012 Jul 04	09:47	M5.3	11515	Multiple Trigger Candidates	$\theta_0 \sim 56^\circ$
19	2012 Jul 05	11:39	M6.1	11515	Complicated Ribbon	...
20	2012 Jul 12	15:37	X1.4	11520	No-precursor Brightening	$\theta_0 \sim 77^\circ$
21	2012 Nov 13	01:58	M6.0	11613	Complicated Ribbon	...
22	2013 Apl 11	06:55	M6.5	11719	No-precursor Brightening	$\theta_0 \sim 52^\circ$
23	2013 Oct 24	00:21	M9.3	11877	Complicated Ribbon	...
24	2013 Nov 01	19:46	M6.3	11884	No-precursor Brightening	$\theta_0 \sim 82^\circ$
25	2013 Nov 03	05:16	M5.0	11884	No-precursor Brightening	$\theta_0 \sim 79^\circ$
26	2013 Nov 05	22:07	X3.3	11890	Complicated Ribbon	...
27	2013 Nov 08	04:20	X1.1	11890	No-precursor Brightening	$\theta_0 \sim 80^\circ$
28	2013 Dec 31	21:45	M6.4	11936	No-precursor Brightening	$\theta_0 \sim 47^\circ$
29	2014 Jan 01	18:40	M9.9	11936	Complicated Ribbon	...
30	2014 Jan 07	10:07	M7.2	11944	No-precursor Brightening	$\theta_0 \sim 95^\circ$
31	2014 Jan 07	18:04	X1.2	11944	No-precursor Brightening	$\theta_0 \sim 15^\circ$
32	2014 Feb 04	03:57	M5.2	11967	Multiple Trigger Candidates	$\theta_0 \sim 65^\circ$

angle of the initially sheared flare ribbons was determined by the averaged angle of the sheared ribbons. We therefore are able to measure the angle only for the events that show two clear flare ribbons in the initial phase. φ_e is the angle perpendicular to the local PIL in the flare-triggering site relative to N .

2.4. Event Selection and Classification Criteria

Following Bamba et al. (2013), we selected events by the criteria summarized below.

1. GOES class was larger than M5.0.
2. Event occurred in the period of 2010 February 11–2014 February 28.
3. The *SDO*/HMI and AIA 1600 Å data covered a period of six hours before and after the flare onset for each event.
4. Flaring site was located within $\pm 750''$ from the solar disk center.

Then we sampled 32 flare events, as summarized in Table 1, and classified the events into six types by evaluating whether the important features I, II, and III of Section 2.1 were observed. The classification procedure and criteria are summarized in Figure 2, and we labeled each type of event as below. The quantitative values of the angles (θ_0, φ_e) stated below were uniquely defined in the present study based on the simulations of K12 for the event classification. Note that we

only measured the angles for the events that showed two clear sheared ribbons and precursor brightenings at a single position; hence, we did not measure the angles for any events classified as the Multiple Trigger Candidates type.

OP Type: The event satisfies the (θ_0, φ_e) condition of the OP type in Figure 2 of K12. In particular, the shear angle and azimuth should satisfy $0^\circ \leq \theta_0 \leq 90^\circ$ and $124^\circ \leq \varphi_e \leq 225^\circ$ at the region/timing where/when the last precursor brightening was seen. Qualitatively, the magnetic field in the small-bipole region has an OP pattern relative to that averaged over the whole AR.

RS Type: The event satisfies the (θ_0, φ_e) condition of the RS type in Figure 2 of K12. In particular, the shear angle and azimuth should satisfy $40^\circ \leq \theta_0$ and $225^\circ \leq \varphi_e \leq 335^\circ$ at the region/timing where/when the last precursor brightening was seen. The RS type has a θ_0 range of approximately 40° – 90° . The local magnetic shear in the small-scale bipole region is toward the opposite direction of the global magnetic shear of the AR.

Contradict-K12 Type: The event occurs with the “no-flare” (θ_0, φ_e) condition in Figure 2 of K12. In particular, $0^\circ \leq \varphi_e \leq 120^\circ$ and $250^\circ \leq \varphi_e$ with a small θ_0 value at the region/timing where/when the last precursor brightening was seen.

Multiple Trigger Candidates Type: The event clearly shows two sheared ribbons (similar to the thick yellow lines in

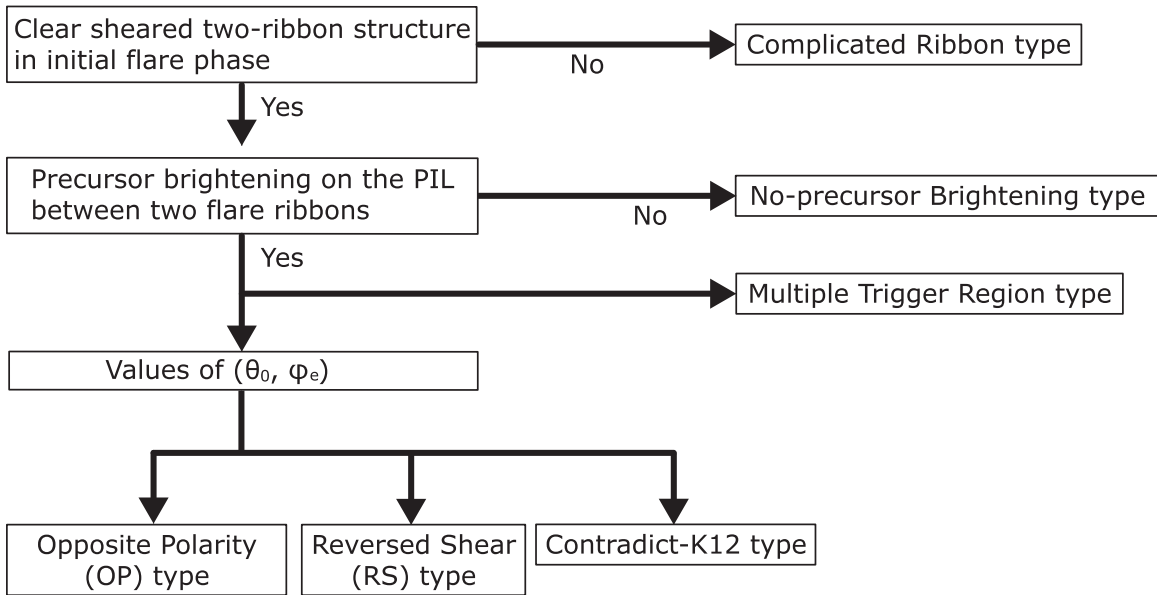


Figure 2. Chart of the classification procedure for the selected events.

Figure 1) in the initial flare phase. However, there are multiple small-scale bipole fields on which precursor brightenings are observed on the local PIL before the flare onset. In other words, there are multiple small-scale bipole fields that show the important features II and III of Section 2.1, before the flare onset.

No-precursor Brightening Type: The event clearly shows two sheared ribbons in the initial flare phase. However, it does not show any precursor brightening over the local PIL of the small-scale bipole field located at the center of the two ribbons, that exists for at least two observation frames (approximately at least over a period of 1.5 minutes) in AIA 1600 Å images from six hours before to the flare onset time. In brief, the event shows only the important structure III of Section 2.1.

Complicated Ribbon Type: The event shows complicated initial flare ribbons that are nothing like the thick yellow lines in Figure 1, i.e., they are much different from feature III suggested by the simulations. More specifically, the flare ribbons seen in the AIA 1600 Å images overplotted on the HMI LOS magnetogram are not able to distinguish its positive and negative polarities during the period from 5 minutes before flare onset to peak time. This type includes cases where flare ribbons appear in parallel (not sheared like Figure 1).

3. Results

The selected flare events and classification results are listed in Table 1, and Table 2 is a summary of the classifications. First, we did not find any events of the Contradict-K12 type. This means that there was no flare event investigated in this study that occurred under “no-flare” combinations of (θ_0, φ_e) and suggests that there was no event that was clearly inconsistent with the flare-trigger conditions proposed by K12, at least among the events investigated in the present study.

Second, 6 of the 32 events satisfied the RS-type condition. Event Nos. 1 and 2 are the same RS-type events examined in

Table 2
Summary of the Event Classification

Type	Number of Events
Opposite Polarity	0
Reversed Shear	6
Contradict-K12	0
Multiple Trigger Candidates	4
No-precursor Brightening	11
Complicated Ribbon	11

previous studies (Bamba et al. 2013, 2014). Figures 3(a-1)–(a-3) show an example of an RS-type event: the X5.4 flare that occurred on 2012 March 7 in AR NOAA 11429. The white/black background indicates the positive/negative polarity of the LOS magnetic field. The green lines and red contours outline the PILs (0 G lines) of the LOS magnetic field and strong emission (2000 DN) in AIA 1600 Å, respectively. The image shows flare ribbons that initially form two clearly sheared ribbon structures on both sides of the PIL, as outlined by black and white broken lines. The yellow arrow indicates the flare-triggering site, and precursor brightenings were intermittently seen in the region, as reported in Bamba et al. (2013, 2014). We measured the magnetic shear angle θ_0 and azimuth φ_e around the flare-triggering site, and the angles were $(\theta_0, \varphi_e) \sim (108^\circ, 313^\circ)$ in the case of the X5.4 flare, as summarized in Table 1. In contrast, there was no OP-type event in our selected sample. Note that Bamba et al. (2013) showed two examples of OP-type events that occurred in 2006, that are out of the time range of this study because the events occurred before the SDO launch.

Third, 4 of the 32 events were classified as multiple trigger candidates type. As an example, the M6.0 flare that occurred on 2011 August 3 in AR NOAA 11261 is shown in Figures 3(b-1)–(b-3). These events showed the important features II and III. However, there were multiple candidates for precursor brightenings at different locations, and a single flare-triggering site could not be identified. In the case of the RS-type events, a precursor brightening is seen at a single location between the initial two ribbons. However, in multiple trigger candidates type

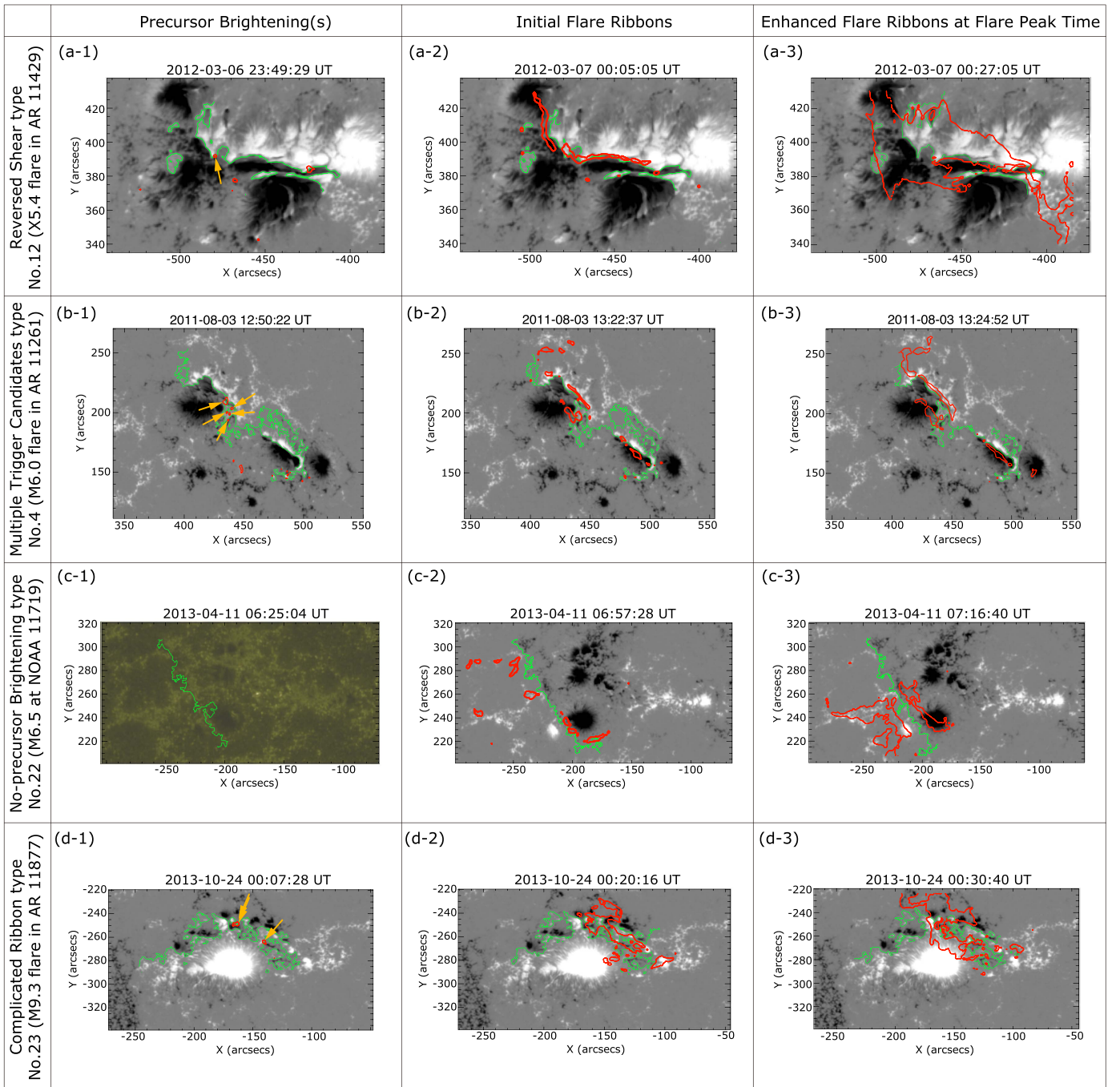


Figure 3. Examples of each event type. Each line and column correspond to the four types and three phases of the flares, as follows. (First line) Reversed shear type: X5.4 flare in AR 11429 (see Movie 1), (second line) multiple trigger candidates type: M6.0 flare in AR 11261 (see Movie 2), (third line) no-precursor brightening type: M6.5 flare in AR 11719 (see Movie 3), and (fourth line) complicated ribbon type: M9.3 flare in AR 11877 (see Movie 4). (First column) Precursor brightening (s), (second column) initial flare ribbons, and (third column) flare peak time. Grayscale represents positive and negative polarities of the LOS magnetograms, which are shown in the range of ± 1000 G, and green lines outline the PILs of 0 G. Red contours plot the initial flare ribbons (2000 DN) seen in AIA 1600 Å images, and yellow arrows in panels (a-1), (b-1), and (d-1) indicate the precursor brightenings for each event. Panel (c-1) shows AIA 1600 Å images 30 minutes before the flare onset because brightenings were not observed on the PIL in the no-precursor brightening type event.

events, precursor brightenings were intermittently seen at several points on the PIL that was in between the two sheared ribbons. Hence, it was difficult to conclude that a single PIL was the flare-triggering site. Moreover, magnetic field structures in the precursor brightening sites were spatially very small in some cases, less than $2''$, which is close to the $1''$ spatial resolution of HMI. In particular, azimuth φ_e , which is measured at the point of

the precursor brightening site, is highly sensitive to the spatial configuration (i.e., the shape of the PIL) of the site. In this study, we chose the flare-triggering sites to be the location where there were precursor brightenings, and, for these cases, it was extremely difficult to measure φ_e at the correct location. Therefore, in this study, we did not measure the angles for these four multiple trigger candidates type events. Note that the

lifetime and spatial size of the precursor brightenings seen in the RS and multiple trigger candidates (and OP) types are different between different events. Bamba et al. (2013) suggested that the critical magnetic flux differs among events because the critical perturbation amplitude needed to trigger the instability depends on how the system is unstable. Related to this, the spatial size and duration of the heating caused by internal reconnection within the trigger field represented by precursor brightenings is different among the events. In addition, empirically from this and other studies (Bamba et al. 2013, 2014; Palacios et al. 2015; Bamba et al. 2017a, 2017b; Wang et al. 2017; Woods et al. 2017), the duration varies from several hours to a few seconds and the spatial sizes were from a few to dozens of arcseconds.

Another noticeable thing is that 22 events were classified as no-precursor brightening or complicated ribbon types. In other words, approximately 70% of the selected events did not show any clear features that were predicted by K12's MHD simulation, such as sheared two-ribbon structure or precursor brightenings. Panels (c-1)–(c-3) show an example of a no-precursor brightening type event: the M6.5 flare that occurred on 2013 April 11 in AR NOAA 118719. The 11 events that are classified as no-precursor brightening types clearly showed a sheared two-ribbon structure in the initial flare phase as suggested by the simulation. However, no brightening was seen on the PIL between the two sheared ribbons, in at least two observation frames (approximately at least over a period of 1.5 minutes), in AIA 1600 Å images, from six hours before to the flare onset time. Many of the no-precursor brightening type events showed similar behavior: that the initial flare ribbons did not widely propagate. The flare ribbons suddenly appeared as bright points, and the intensity became enhanced at almost the same location within a few minutes. Panels (d-1)–(d-3) show an example of the complicated ribbon type: the M9.3 flare that occurred on 2013 October 24 in AR NOAA 11877. Initially the flare ribbons had a complex shape or sometimes looked almost like a single ribbon.

Here, we briefly summarize the classification results.

1. There was no Contradict-K12 type event that satisfied the “no-flare” condition of K12.
2. 30% of the events, including six RS-type events and four multiple trigger candidates types, were consistent with K12.
3. Approximately 70% of the events (22 of the analyzed 32 events) were classified as either the no-precursor brightening or complicated ribbon types that did not clearly show the key features suggested by K12.

4. Discussion

The result that 70% of the events did not show the key features suggested by the MHD simulation of K12 is interesting. Therefore, we discuss here whether the events classified as complicated ribbon and no-precursor brightening types could be explained by K12's model or by other models.

4.1. Complicated Ribbon Type

It is not surprising that many of the flares showed complicated flare ribbons because the coronal magnetic fields are naturally intertwined. Figure 4 shows a time series analysis of the M5.6 flare (No. 17 listed in Table 1) that occurred on

2012 July 2 in AR NOAA 11515, which was classified as a complicated ribbon type. The M5.6 flare occurred in a weak negative polarity region between the leading sunspot (LS) and the satellite spot (SS). The red contour in panel (e) shows the initial flare ribbon of the M5.6 flare, but it is very different from the sheared two-ribbon structure, which is suggested by K12's simulation (illustrated by the thick yellow line in Figure 1). The M5.6 flare followed a filament eruption and the preceding C2.9 flare whose flare ribbons are seen in Figure 4(d) in the same region, as Louis et al. (2014) reported. The filament was rooted in the rear part of the LS and weak negative region, as illustrated in Figures 4(a) and (b) by blue arcs.

We found a tiny brightening near the southern root of the filament (the region surrounded by the yellow square in Figures 4(a) and (b)) over a small wedge-like structure, as can be seen in the enlarged image in panel (a), and it started from 10:10 UT on 2012 July 2. The brightening region gradually extended (as seen in panel (b)), and the C2.9 flare occurred at 10:33 UT (panel (c)). The flare ribbons of the C2.9 event were also complicated as seen in panel (d). The M5.6 flare started at 10:43 UT (panel (e)) from a region slightly to the northwest of the C-class flaring region. Then two clear ribbons (PR and NR) appeared as sheared ribbons in the latter phase (panel (f)). We measured the angles θ_0 and φ_e before the C2.9 flare and eruption onset, assuming that the large-scale magnetic field structure around the SS had not drastically changed. The result of the measurement was $(\theta_0, \varphi_e) \sim (126^\circ, 351^\circ)$, and it is consistent with the RS type condition. From the result, we were able to conclude that the M5.6 flare was triggered by the RS-type magnetic field structure in a three-step process, including the C2.9 flare and the filament eruption.

Bamba et al. (2017a) also identified the flare-triggering site for an X1.0 flare, which showed three complicated flare ribbons in the initial phase and can be classified as a complicated ribbon type, through a detailed analysis. They suggested that precise analyses of spatial and temporal relationships between magnetic field structures and overlying structures such as filaments and precursor brightenings are effective for identifying the flare-triggering site for the complicated ribbon-type event. Furthermore, Bamba et al. (2017b) confirmed by spectroscopic observation that precursor brightenings can be a marker of magnetic reconnection in the lower atmosphere, such as the internal magnetic reconnection proposed by K12. We hence investigated whether precursor brightenings were seen on a PIL in the region where flare ribbons appeared with regards to the complicated ribbon-type events. Table 3 shows a list of the complicated ribbon-type events and whether precursor brightenings exist or not. Brightenings on a PIL were observed in 8 out of the 11 complicated ribbon-type events. Accordingly, we propose that it is possible that the flare-triggering site for the eight events may be found through a detailed analysis, and we need a precise analysis for each individual event.

On the other hand, we should further consider the relationship between the complicated ribbon-type events and a flare-trigger by magnetic reconnection at a coronal null point (Longcope 2005; Titov 2007; Titov et al. 2009). The flare ribbons of the above M5.6 flare (seen in Figure 4(f)) look like the circular-shaped ribbons, such as those studied by, for example, Masson et al. (2009). Complex circular-shaped or scattered flare ribbons distributed from a coronal null point origin may be possible in this case.

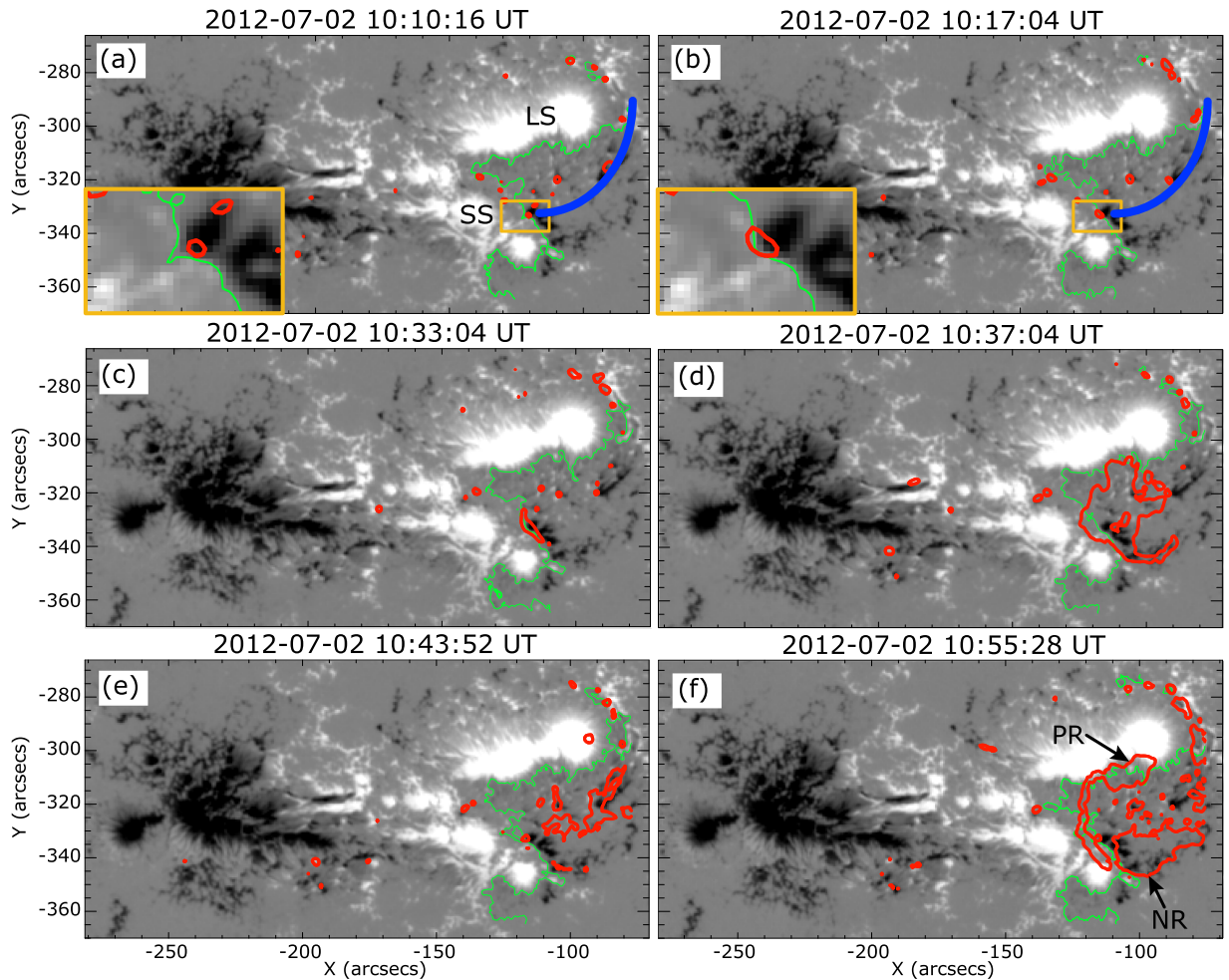


Figure 4. Example of the complicated ribbon type: the M5.6 flare in 2012 July 2 in AR NOAA 11515. The images are formatted as in Figure 3. Thick-blue arcs roughly represent the shape and location of a filament that is seen in $H\alpha$ images (see Louis et al. 2014). The southern root of the filament is surrounded by yellow rectangles and enlarged in the bottom left in panels (a) and (b). A tiny brightening was seen over the PIL within the enlarged region.

4.2. No-precursor Brightening Type

With regard to the events that did not cause precursor brightenings, such as the no-precursor brightening type and three of the complicated ribbon-type events, the possibility that the flares were triggered by a different physical process(es) from that proposed by K12 cannot also be ruled out. K12 proposed that major flares should be preceded by internal magnetic reconnection between the flare-triggering flux of the OP or RS types and pre-existing sheared magnetic field. They treated precursor brightenings in the lower atmosphere on the flare-triggering site as a proxy of the internal reconnection. Therefore, we still can consider other physical process(es). For instance, if a long twisted flux rope was strapped down by an overlying magnetic field and the trapping field was weakened by some cause such as emerging flux (case-B scenario of Chen & Shibata 2000), then, in this case, precursor brightenings may be seen at a footpoint of the trapping field, which may be away from the flaring site. We should confirm the existence of a long twisted flux rope, and investigate how the flux rope was formed during the AR evolution, using observational data at high temperature, such as that taken by the *Hinode*/X-ray telescope. Otherwise, gradual magnetic flux cancellation at a footpoint of the overlying field may also weaken the trapping field (van Ballegoijen & Martens 1989; Zhang et al. 2001; Green

et al. 2011). Precursor brightenings may be observed if the flux cancellation was caused by magnetic reconnection between OP fluxes. However, it is conceivable that no brightening may be observed in the case of flux cancellation by sinking of small magnetic fluxes in the photosphere. Another possibility for the no-precursor brightening event is that a magnetic flux tube had formed in advance by something, such as a preceding flare or photospheric motion, and it became unstable to the ideal MHD instabilities of torus, kink, and double-arc modes (Török & Kliem 2005; Kliem & Török 2006; Ishiguro & Kusano 2017).

We note that there may be a possibility that precursor brightenings can be seen in a different wavelength from AIA 1600 Å, which was used in the present study and is sensitive to emission from the upper photosphere and lower transition region ($\log T \sim 5.0$). In particular, in the case of the RS type, magnetic shear cancellation by internal reconnection could occur at any altitude, while the internal reconnection should occur in the lower atmosphere in the OP-type case. This is because the altitude of the internal reconnection in the RS-type case depends on the spatial size of the pre-existing sheared field and flare-trigger field. Therefore, it might be likely that we cannot detect internal reconnection of the RS type by emission in 1600 Å, if the internal reconnection proceeds in the coronal region. We can also consider the breakout trigger scenario (Antiochos et al. 1999), in which magnetic reconnection occurs

Table 3
List of the Complicated Ribbon-type Events and Precursor Responses

No.	Date	Onset Time (UT)	GOES X-ray Class	NOAA AR	Precursor Brightenings ^a
3	2011 Mar 09	23:13	X1.5	11166	Yes
5	2011 Aug 04	03:41	M9.3	11261	Yes
8	2011 Sep 07	22:32	X1.8	11283	No
9	2011 Sep 08	15:32	M6.7	11283	Yes
16	2012 May 10	04:11	M5.7	11476	No
17	2012 Jul 02	10:43	M5.6	11515	Yes
19	2012 Jul 05	11:39	M6.1	11515	Yes
21	2012 Nov 13	01:58	M6.0	11613	Yes
23	2013 Oct 24	00:21	M9.3	11877	Yes
26	2013 Nov 05	22:07	X3.3	11890	Yes
29	2014 Jan 01	18:40	M9.9	11936	No

Note.

^a Precursor brightenings were seen in AIA 1600 Å in at least two frames (i.e., at least over a period of ~ 1.5 minutes) from one hour before to the flare onset.

at much higher altitude than that focused on in this study. Precursor brightenings may be observed in higher temperature lines than AIA 1600 Å as in the RS-type case event. Another possibility is that the size of the internal reconnection region working as a trigger was too small to be observed. Recently, Ishiguro & Kusano (2017) developed a theoretical model of the new double-arc instability, and, according to that model, they predict that the size of the triggering reconnection depends on the strength of the magnetic twist. If magnetic twist is high enough, even tiny reconnection can trigger the double-arc instability and work as a flare trigger. Therefore, it is necessary to distinguish which types of flares are caused by which physical process, i.e., which types of flares are explained by which model, by more precisely analyzing each of the events using multiple wavelengths data.

4.3. Multiple Trigger Candidates Type

The multiple trigger candidates type events, in which there were several flare-triggering site candidates, is still understandable by the flare-trigger model of K12. It is not necessary to restrict the number of flare-triggering sites for some cases. Bamba et al. (2013, 2014) suggested that not only the geometrical conditions θ_0 and φ_e but also the total magnetic flux in the flare-triggering site and/or its temporal evolution contribute to the critical conditions for flare occurrence. They also suggested that the critical magnetic flux required to trigger an instability depends on the proximity of the system to an unstable state. Hence the combined contribution of more than one small-scale flux, that satisfies either the OP- and/or RS-type condition, is also conceivable as a flare trigger. Bamba et al. (2017b) analyzed a region that includes two RS-type bipole structures and studied the sequential process from the internal reconnection, which was represented by precursor brightenings, to the destabilization of the large-scale system in the AR, using spectroscopic data. However, they were not able to determine the detailed process by which the two flare-triggering sites contributed to the flare occurrence because the data they employed only covered the odd RS-type region. Thus, we need more analyses to clarify the combination effect of multiple and different types of trigger regions. These no-precursor brightening and multiple trigger candidates type events are future topics of discussion.

4.4. Difference of the Incidence Rate of OP and RS Types

Another interesting topic for discussion is the result that the OP-type events were rare compared to the RS types, at least in this study. Some other studies found events that were suggested to be triggered by the OP-type small magnetic structure (Palacios et al. 2015; Wang et al. 2017; Woods et al. 2017). However, so far, we found only two OP-type flare events (already shown by Bamba et al. 2013 by the same method of this study), whereas six events were classified as RS types in this study. We consider that the difference in incidence between the two types results from a difference of flexibility in the geometrical conditions, such as displacement of the flare-trigger field from the highly sheared PIL and the height of the internal reconnection. For instance, the internal reconnection in the RS type case may be less sensitive to altitude, and it can occur more frequently than internal reconnection triggered by the OP-type structure. Otherwise, the RS-type case may be sensitive to displacement of the flare-triggering site from the highly sheared (flaring) PIL.

In the OP-type case, pre-existing, large-scale, magnetic arcades (red arcades in Figure 1) should directly reconnect with the flare-trigger field (blue arcade in Figure 1) in order to form long twisted flux ropes. Therefore, the twisted flux rope, which will erupt and trigger flare reconnection, could not be formed if the small bipole is away from the PIL. Conversely, in the RS-type case, magnetic shear cancellation, i.e., the internal magnetic reconnection between the pre-existing magnetic field (red arcades in Figure 1) and the trigger field (the blue arcade in Figure 1), can occur as long as the small bipole exists under the pre-existing sheared magnetic arcades. Thus, the sheared magnetic arcades can collapse and flare reconnection can be triggered by shear cancellation as long as the RS-type field exists within the sheared arcade even if it is located away from the PIL. From observational results, such as those reported by Bamba et al. (2017a), it is also suggested that the RS-type flare-trigger could work even if it is located slightly away from the flaring PIL, even though the trigger field was injected just above the PIL in the K12 simulations.

Therefore, the differences in sensitivity to the geometrical conditions and incidence are originally derived from differences in the physical processes for flare-triggering between the two types. Thus it is not surprising that the OP-type flare trigger is more rare than the RS-type flare trigger. However, it is still unclear how a distant field that is away from the PIL can trigger

flares in the OP and RS cases on the actual solar surface, and we need to statistically investigate the distance between flaring PILs and flare-trigger fields using observational data.

5. Summary

In this study, we aimed to evaluate the consistency between the theoretical flare-trigger model of K12 and a variety of major flares that occurred on the actual solar surface, by focusing on the geometrical structure. We selected 32 major flares and tried to identify the flare-triggering site by applying the analysis method that was developed by Bamba et al. (2013, 2014) to *SDO*/HMI LOS magnetograms and AIA 1600 Å images. We classified the 32 events into six types of groups including K12's OP and RS types.

The most noteworthy result is that 30% of the events (including the RS-type events and multiple trigger candidates type) were consistent with K12. Moreover, there was no event that contradicted K12 and satisfied their “no-flare” condition at least in the events sampled in this study. Of the 11 complicated ribbon type events, 8 could be interpreted by K12's flare-trigger model, even though we need a more precise analysis of the spatial and temporal relationships between the magnetic field and overlying structures such as filament and precursor brightenings. Meanwhile, we found that there is a possibility that different physical process(es) from those proposed by K12 cannot also be ruled out for the events that did not show any precursor brightenings, such as the no-precursor brightening type events and the three complicated ribbon type events. We still can consider other physical processes such as the emerging flux model proposed by Chen & Shibata (2000) and the magnetic flux cancellation model proposed by van Ballegoijen & Martens (1989), Zhang et al. (2001), and Green et al. (2011), to trigger these events. Extended studies are required to reveal the physical process(es) that cause the different types of flares. Even so, our result that 30% of the events investigated in this study were consistent with the flare-trigger model of K12 leads to the conclusion that the observable features and (θ_0, φ_e) parameters of K12 are important to understand the flare triggering.

Moreover, we found that there was no OP-type event in the events analyzed in this study, while there were six RS-type events. We hypothesized that this difference of incidence between the OP and RS types is likely owing to differences in the physical processes between the two types: the RS-type condition can be satisfied more easily because the geometrical conditions of the RS type are more flexible than those of the OP type. We need an extended study to clarify the occurrence difference between the OP and RS types, and the consistency/inconsistency between the complicated ribbon type, no-precursor brightening type, and multiple trigger candidates type events and the physical flare-trigger process of K12. In particular, it is important to comprehensively analyze the relationship between the photospheric magnetic field structures and chromospheric/coronal features, using not only AIA 1600 Å images but also multiple wavelengths. Moreover, we caution that the limitations of this study given the single UV wavelength used, and relying upon the LOS magnetic field data for the PIL location in AIA images, may introduce bias and errors in the results and their interpretation (see the Appendix). As such, it is suggested that a further study be performed using additional data and more careful analysis. We should reveal the role of the small-scale OP- or RS-type fields for a flare in

various magnetic field topologies, using both simulations and precise observations.

The authors deeply appreciate the many instructive comments and encouragement from Dr. K. D. Leka, Dr. Satoshi Inoue, Dr. David H. Brooks, Dr. Shinsuke Imada, and researchers in ISAS/JAXA and NAOJ. The authors thank Dr. T. Hara for providing the data analysis tool. The HMI and AIA data have been used through the courtesy of NASA/*SDO* and the AIA and HMI science teams. This work was partly carried out at the *Hinode* Science Center at NAOJ and Nagoya University, Japan, and the Solar Data Analysis System (SDAS) operated by the Astronomy Data Center in cooperation with the *Hinode* Science Center of the NAOJ. This work was supported by MEXT/JSPS KAKENHI grant Nos. JP16H07478, JP15H05812, JP15K21709, JP15H05814, and JP15J10092. The authors thank the anonymous referee for valuable comments that improved the clarity of the manuscript.

Appendix

Caveat of Using the LOS Magnetic Field Data to Detect the Flare-triggering Site

In this study, we mainly used the HMI LOS magnetograms to investigate the photospheric magnetic field structures. The LOS magnetic field contains a projection-effect, that is, the LOS component of the magnetic field B_{LOS} can be treated as the radial component B_r only when the observing angle θ equal 0 (or $\mu = \cos(\theta) = 1.0$). In other words, B_r can be different from B_{LOS} depending on the location of the AR on the solar surface, even very close to solar disk center (Leka et al. 2017). In this study (also Bamba et al. 2013, 2014), events were selected based on the criterion that the flaring site was located within $\pm 750''$ of the solar disk center ($\mu \sim 0.67$), in consideration of this projection effect.

However, we should keep in mind that there is a possibility that we may get a slightly different result between the analysis with B_{LOS} and with B_r . The flare-trigger field can be a very small-scale structure (empirically estimated as dozens of megameters) compared to the spatial size of an AR, and the spatial size of the trigger field is different between different AR. Moreover, the azimuth φ_e is highly sensitive to the configuration of the local PIL and the location of the precursor brightenings in the flare-triggering site. We should have an extended analysis (a future work) using B_r instead of B_{LOS} to clarify the consistency between the flare-trigger model of K12 and the events classified as multiple trigger candidates, no-precursor brightening, and complicated ribbon types.

We also used SHARP data, converted into Lambert CEA projection, to measure the shear angle θ_0 in the present study. The magnetic field vectors in SHARP data have been transformed into components of the heliographic coordinates (B_r, B_θ, B_ϕ) , which were originally in a spherical coordinate system, and these are transformed into a planar CEA coordinate system. These unit vectors in each coordinate system are not precisely aligned except at the center of the patch. In fact, an error is caused when the vectors are transformed from a spherical coordinate system to a planar CEA coordinate system (Bobra et al. 2014). In this study, we determined the flaring PIL with coaligned B_{LOS} and AIA 1600 Å images; however, it may not match the PIL identified using SHARP CEA data. We could have a few-pixel shift in the location of the PIL depending on the location of the AR on the solar surface. Therefore, we

averaged the angle θ_0 over a region 5–10 times the area of the flare-trigger field.

ORCID iDs

Kanya Kusano  <https://orcid.org/0000-0002-6814-6810>

References

- Antiochos, S. K., DeVore, C. R., & Klimchuk, J. A. 1999, *ApJ*, **510**, 485
- Aulanier, G., Török, T., Démoulin, P., & DeLuca, E. E. 2010, *ApJ*, **708**, 314
- Bamba, Y., Inoue, S., Kusano, K., & Shiota, D. 2017a, *ApJ*, **838**, 134
- Bamba, Y., Kusano, K., Imada, S., & Iida, Y. 2014, *PASJ*, **66**, S16
- Bamba, Y., Kusano, K., Yamamoto, T. T., & Okamoto, T. J. 2013, *ApJ*, **778**, 48
- Bamba, Y., Lee, K.-S., Imada, S., & Kusano, K. 2017b, *ApJ*, **840**, 116
- Bateman, G. 1978, *MHD Instabilities* (Cambridge, MA: MIT Press)
- Bobra, M. G., & Couvidat, S. 2015, *ApJ*, **798**, 135
- Bobra, M. G., Sun, X., Hoeksema, J. T., et al. 2014, *SoPh*, **289**, 3549
- Carmichael, H. 1964, *NASSP*, **50**, 451
- Chen, P. F., & Shibata, K. 2000, *ApJ*, **545**, 524
- Cheng, X., Zhang, J., Ding, M. D., Guo, Y., & Su, J. T. 2011, *ApJ*, **732**, 87
- Démoulin, P., & Aulanier, G. 2010, *ApJ*, **718**, 1388
- Falconer, D. A., Moore, R. L., & Gary, G. A. 2008, *ApJ*, **689**, 1433
- Fan, Y., & Gibson, S. E. 2003, *ApJ*, **609**, 1123
- Gerrard, C. L., Arber, T. D., Hood, A. W., & Van der Linden, R. A. M. 2001, *A&A*, **373**, 1089
- Green, L. M., Kliem, B., & Wallace, A. J. 2011, *A&A*, **526**, A2
- Hagyard, M. J., Moore, R. L., & Emslie, A. G. 1984a, *AdSpR*, **4**, 71
- Hagyard, M. J., Teuber, D., West, E. A., & Smith, J. B. 1984b, *SoPh*, **91**, 115
- Hassanin, A., & Kliem, B. 2016, *ApJ*, **832**, 106
- Higgins, P. A., Gallagher, P. T., McAteer, R. T. J., & Bloomfield, D. S. 2011, *AdSpR*, **47**, 2105
- Hirayama, T. 1974, *SoPh*, **34**, 323
- Ishiguro, N., & Kusano, K. 2017, *ApJ*, **843**, 101
- Karpen, J. T., Antiochos, S. K., & DeVore, C. R. 2012, *ApJ*, **760**, 81
- Kliem, B., Lin, J., Forbes, T. G., Priest, E. R., & Török, T. 2014, *ApJ*, **789**, 46
- Kliem, B., Su, Y. N., van Ballegooijen, A. A., & DeLuca, E. E. 2013, *ApJ*, **779**, 129
- Kliem, B., & Török, T. 2006, *PhRvL*, **96**, 255002
- Kopp, R. A., & Pneuman, G. W. 1976, *SoPh*, **50**, 85
- Kosugi, T., Matsuzaki, K., Sakao, T., et al. 2007, *SoPh*, **243**, 3
- Kusano, K., Bamba, Y., Yamamoto, T. T., et al. 2012, *ApJ*, **760**, 31
- Leka, K. D., Barnes, G., & Wagner, E. L. 2017, *SoPh*, **292**, 36
- Lemen, J. R., Title, A. M., Akin, D. J., et al. 2012, *SoPh*, **275**, 17
- Liu, C., Deng, N., Lee, J., et al. 2013, *ApJL*, **L36**
- Liu, R., Kliem, B., Titov, V. S., et al. 2016, *ApJ*, **818**, 148
- Longcope, D. W. 2005, *LRSP*, **2**, 7
- Louis, R. E., Puschmann, K. G., Kliem, B., Balthasar, H., & Denker, C. 2014, *A&A*, **562**, A110
- Masson, S., Pariat, E., Aulanier, G., & Schrijver, C. J. 2009, *ApJ*, **700**, 559
- Moore, R. L., & Sterling, A. C. 2006, *GMS*, **165**, 43
- Moore, R. L., Sterling, A. C., Hudson, H. S., & Lemen, J. R. 2001, *ApJ*, **552**, 833
- Palacios, J., Cid, C., Guerrero, A., Saiz, E., & Cerrato, Y. 2015, *A&A*, **583**, A47
- Pesnell, W. D., Thompson, B. J., & Chamberlin, P. C. 2012, *SoPh*, **275**, 3
- Priest, E. R., & Titov, V. S. 1996, *RSPSA*, **354**, 2951
- Reva, A. A., Ulyanov, A. S., Shestov, S. V., & Kuzin, S. V. 2016, *ApJ*, **816**, 90
- Savcheva, A., Pariat, E., McKillop, S., et al. 2015, *ApJ*, **810**, 96
- Schmieder, B., Aulanier, G., & Vršnak, B. 2015, *SoPh*, **290**, 3457
- Schou, J., Scherrer, P. H., Bush, R. I., et al. 2012, *SoPh*, **275**, 229
- Schrijver, C. J. 2007, *ApJL*, **655**, L117
- Sturrock, P. A. 1966, *Natur*, **211**, 695
- Sun, X., Hoeksema, J. T., Liu, Y., Chen, Q., & Hayashi, K. 2012, *ApJ*, **757**, 149
- Titov, V. S. 2007, *ApJ*, **660**, 863
- Titov, V. S., Forbes, T. G., Priest, E. R., Mikić, Z., & Linker, J. A. 2009, *ApJ*, **693**, 1029
- Török, T., & Kliem, B. 2005, *ApJL*, **630**, L97
- Török, T., Kliem, B., & Titov, V. S. 2004, *A&A*, **413**, L27
- van Ballegooijen, A. A., & Martens, P. C. H. 1989, *ApJ*, **343**, 971
- Wang, H., Liu, C., Ahn, K., et al. 2017, *NatAs*, **1**, 0085
- Woods, M. M., Harra, L. K., Matthews, S. A., et al. 2017, *SoPh*, **292**, 38
- Zhang, J., Wang, J., Deng, Y., & Wu, D. 2001, *ApJL*, **548**, L99
- Zuccarello, F. P., Aulanier, G., & Gilchrist, S. A. 2015, *ApJ*, **814**, 126